Materials Science & Engineering A 713 (2018) 81–93

Contents lists available at ScienceDirect

Materials Science & Engineering A

journal homepage: www.elsevier.com/locate/msea

Origin of plastic anisotropy in (ultra)-fine-grained Mg–Zn–Zr alloy processed by isothermal multi-step forging and rolling: Experiments and modeling

Dayan Nugmanov[a,c,*], Marko Knezevic[b,**], Milovan Zecevic[b], Oleg Sitdikov[c], Michael Markushev[c], Irene J. Beyerlein[d]

[a] Institute of Nanotechnology, Karlsruhe Institute of Technology, Karlsruhe 76021, Germany
[b] Department of Mechanical Engineering, University of New Hampshire, Durham, NH 03824, USA
[c] Institute for Metals Superplasticity Problems of Russian Academy of Sciences, Ufa 450001, Russia
[d] Mechanical Engineering Department, Materials Department, University of California at Santa Barbara, Santa Barbara, CA 93106, USA

ARTICLE INFO

Keywords:
Magnesium alloys
Multi-step isothermal forging
Rolling
Texture
Anisotropy

ABSTRACT

This paper reports a strong effect of multi-step forging (MIF) followed by elevated temperature isothermal rolling (IR) on the yield stress in ZK60 Mg alloy. After the MIF stage, the yield stress is slightly higher in the rolling direction (RD) than in the transverse direction (TD). After IR at 300 °C, the anisotropy remains small. In contrast, after IR at a lower temperature 200 °C, a significant difference in yield stress between the RD and TD directions is observed, found to increase with rolling strain, and even reverse from being higher to being much lower in the RD than in the TD with rolling reduction at 200 °C. To help determine the possible causes for the anisotropy and its evolution with straining, we use a multi-scale elasto-plastic self-consistent polycrystal model that accounts for dislocation density (Taylor hardening), precipitate hardening, texture, and grain size. The model is extended here to also include the effects of type I and type II residual stresses. With a combination of modeling and electron microscopy, we find that texture, grain size distribution, residual stresses, Taylor hardening, and Orowan hardening only have moderate effects on the plastic anisotropy and cannot fully explain the observations. We rationalize that the primary origin of the yield anisotropy is the evolution of the secondary precipitates, which become distributed in the plane of the rolled sheet during rolling. They become more aligned in the RD plane during IR, causing strengthening in tensile yield stress in the TD over that in the RD.

1. Introduction

Magnesium alloys are being increasingly investigated for many applications in the automotive, aerospace and electronic device industries because of their high specific strength [1–4]. Due to low-symmetry hexagonal lattice structure, preferred crystallographic texture development during processing, and possible activation of only a few slip and twin modes at room temperature, these alloys exhibit limited cold workability [5–7]. Their ambient temperature plastic flow predominantly occurs on the basal and prismatic slip planes (with the former usually easier) and extension twinning [8–12]. The latter are microstructural inhomogeneities that create large lattice reorientations, barriers to dislocation motion, as well as introduce local stress fields, and hence often result in pronounced plastic anisotropy [13,14]. The activation of pyramidal $< \mathbf{c}+\mathbf{a} >$ slip systems provides the additional degree of freedom needed for an arbitrary isochoric plastic strain, and has been confirmed experimentally but requires a higher driving force [15]. Such deformation behavior is more applicable to conventional coarse-grained (CG) Mg alloys. Ultra-fine and fine-grained (UFG and FG) materials with the grain sizes less than 1 and 10 μm, respectively, can exhibit even more directional mechanical properties, as well as an early material failure [1]. Moreover, strength of these materials can be enhanced due to grain refinement, when the homogeneity in the spatial distribution of fine grain size is important [16]. A majority of commercial Mg alloys have a pseudo-single phase structure, since they are comprised of a solid solution Mg matrix with primary (excess phase particles formed during liquid state solidification) and secondary (phase precipitated from supersolid solution during alloy heat or thermomechanical treatment in two-phase region) phases. The behavior of Mg alloys can be influenced by a non-uniform (anisotropic) distribution of these phases. The small secondary precipitates can significantly contribute to the strength of the material [17].

Many recent studies have shown that multi-step isothermal forging (MIF) combined with isothermal rolling (IR) can be an effective

* Corresponding author.
** Correspondence to: Department of Mechanical Engineering, University of New Hampshire, 33 Academic Way, Kingsbury Hall, W119, Durham, NH 03824, USA.
E-mail addresses: dnugmanov@gmail.com (D. Nugmanov), marko.knezevic@unh.edu (M. Knezevic).

https://doi.org/10.1016/j.msea.2017.12.045
Received 20 October 2017; Accepted 11 December 2017
Available online 13 December 2017
0921-5093/

technique for creating UFG sheets and can advantageously be accomplished with the use of conventional tooling and hydraulic presses [16,18,19]. The MIF + IF formed UFG sheets have refined grains, texture development and directionally shaped precipitates. Mechanical testing have found Hall-Petch-like isotropic hardening [20,21], plastic anisotropy [22,23], and texture softening [20,24]. While some of these attributes can be desirable, such as strengthening, the underlying mechanisms that lead to these effects need to be better understood in order to enable widespread use and their eventual incorporation into commercial applications.

A number of studies have been conducted to assess the effect of texture [25,26] and precipitates [27,28] on the critical resolved shear stress (CRSS) values and activity of different slip and twinning modes in Mg alloys. For example, Lentz and al. [29,30] reported a reduction in the critical resolved shear stress (CRSS) for extension twinning (TTW) and $< \mathbf{c}+\mathbf{a} >$ pyramidal slip due to precipitates in the Mg-Y-Nd alloy during tension. As another example, rolling and annealing Mg alloys can result in the formation of a strong basal texture, where basal and prismatic slip systems have zero or low Schmid factor when deformed in the through-thickness direction of the rolled sheet. In this case, the deformation can be accommodated by the activation of pyramidal slip or contraction twinning. Since twinning can only accommodate a small portion of the strain and the $< c+a >$ pyramidal slip is relatively hard, the material response was much harder than, for example, that in the in-plane compression, where grains were more suitably oriented for the softer basal slip and easier extension twinning. However, strength anisotropy can change due to the effect of precipitates and the UFG structure. The CRSS for basal slip mode in Mg should be lower than for prismatic slip mode. Nevertheless, in fine-grained Mg alloys it was shown that basal and prismatic slip have similar activity and their CRSS is almost equal [31–33]. Similar findings have been reported for Zr/Nb composites [34].

Precipitate particles are exploited for strengthening in many Mg alloys [1]. The precipitates that form mainly take the form of rods or plates and sometime spheres, lying on particular crystallographic planes. The shape and the plane containing the precipitate depend on the alloy system and thermal treatment [35]. It is known that different precipitate types lead to markedly different strengthening. For example, the basal plates formed in Mg–Al–Zn (AZ) alloys generally give poor strengthening, while the prismatic plates that form in Mg–Y–RE (rare earth) alloys, such as WE54, provide a high level of strengthening [29,36]. Also precipitates can enhance or reduce the degree of asymmetry and anisotropy depending on their shape.

In many Mg alloys, as well as the Mg alloy of interest in the present work ZK60, the precipitates are too large to form coherent interfaces with the matrix and to be cut by dislocations. The influence of precipitate shape on strength is therefore assumed to depend on the Orowan stress required to bow dislocations around the particles. Two strengthening phases in Mg-Zn alloys are β_1' that have a base-centered monoclinic structure and β_2' that have a hexagonal structure similar to that of $MgZn_2$ [37]. These phases have different morphologies. β_1' develop in the form of rods with an axis parallel to [0001], while β_2' form as plates on the (0001) plane [37]. Rod-shape and plate-shape precipitates in static annealing strongly orient their long axis in one crystallographic direction in each grain [26,27,33,34]. The presence of these anisotropic precipitates can, therefore, harden one crystallographic deformation mode more than another depending on their orientation relationship. Using a mean-field polycrystal plasticity model, it was shown in prior work that β_1' in form of rods hardened the prismatic slip systems and twin systems more than the basal slip systems [38]. In another study [39], it was concluded that β_1' precipitates were not effective in increasing the strength of the material when the load is applied perpendicular to c-axis. An investigation of the effect of plate-like particles lying on the basal plane in AZ91 showed that the prismatic slip mode experienced significantly larger increase in CRSS compared to the basal slip mode [40].

To aid in understanding microstructural effects on constitutive response, self-consistent (SC) polycrystal models, such as visco-plastic self consistent (VPSC) and elasto-plastic self consistent (EPSC), have been developed to account for a number of subgrain level phenomena that together are responsible for so-called hardening, the increase in the resistance to slip on crystallographic slip planes with increasing strain. Hardening has been modeled via phenomenological laws, such as the Voce law and mechanical threshold stress [41,42], or based on the evolution of statistically stored dislocations [35,43–46], as well as both stored and geometrically necessary dislocations [47,48]. Although more challenging, representing the effects of deformation twinning along with slip has also been accomplished in these models, with the use of two-phase models and transfer volume schemes as parts of the matrix transforms into twins. Recently, VPSC and EPSC models have been advanced to concurrently calculate the evolution of texture and twin fraction during twinning and de-twinning in hexagonal metals [49,50]. The EPSC model further predicts the evolution of lattice strains, which is useful for interpreting diffraction data.

The present work combines a recent version of the EPSC model and electron microscopy to study the origin of anisotropy of ZK60 alloy processed by MIF and IR. After MIF, the material exhibited an FG structure with a split basal texture tilted towards the rolling direction (RD) for approximately 45–50° [51]. The grain structure slightly changed after isothermal rolling (IR) and became a combination of UFG and FG [52], but the basal texture formed during IR. We find a significant yield strength anisotropy at room temperature after MIF as well as after the subsequent IR processes for the three strain levels used. Microscopic evaluation finds that the coarse particles in longitudinal and transverse cross-sections appear compact and similarly distributed due to MIF carried out. Thus, the excess phases have a very slight effect on strain hardening and in-plane anisotropy. The EPSC modeling suggests that texture, grain size distribution, residual stresses, Taylor hardening, and Orowan hardening from the large coarse second-phase particles were not responsible for the yield anisotropy. With further analysis, we show that the strong anisotropy in yield stress is due to an anisotropic distribution of small (< 500 nm) secondary precipitates. These submicron-sized precipitates can be classified into two types: ones that lie in the RD-ND (normal direction) plane and another lying in the TD (transverse direction)-ND plane. The maximum diameter of the former is larger than that of the latter.

2. Material and experiments

2.1. Material and processing

The material used in this work is the ZK60 (Russian MA14) Mg alloy (Mg-6Zn-0.6Zr). It started as billets machined from a commercial hot-pressed rod 90 mm in diameter and 170 mm in length. For study, the billets were processed by a multistage metals forming process called, MIF, and subsequently by isothermal rolling (IR) to three rolling reductions. The MIF process was performed using a hydraulic press with the isothermal die set. Fig. 1a shows the three sequential steps used in MIF at 400 °C, 300 °C and 200 °C. Each MIF step consisted of several cycles, some of which involved changing the axis (as shown in Fig. 1b) [25,26,44,45]. Specifically the first step was cylinder upsetting (shown in the first image of Fig. 1b). Next, the second upsetting was from the side rib (shown in the second image of Fig. 1b). As a result, the series of MIF cycles produced a billet with a square cross-section elongated in the X-direction. The billet dimensions after MIF in mm were 70 × 70 × 170. The true strain accumulated in each step is 4.2 at 400 °C, 3.0 at 300 °C and 3.0 at 200 °C. The total number of MIF cycles was 18 leading to a total true strain of $e = 10.2$. This MIF process was carried out to much larger strain levels than before. Prior work found that strains below the level of 3 were not sufficient for achieving grain refinement.

The subsequent IR step was carried out at 200 °C and 300 °C (Fig. 1c). In this process, the billet is rolled in the X-direction to

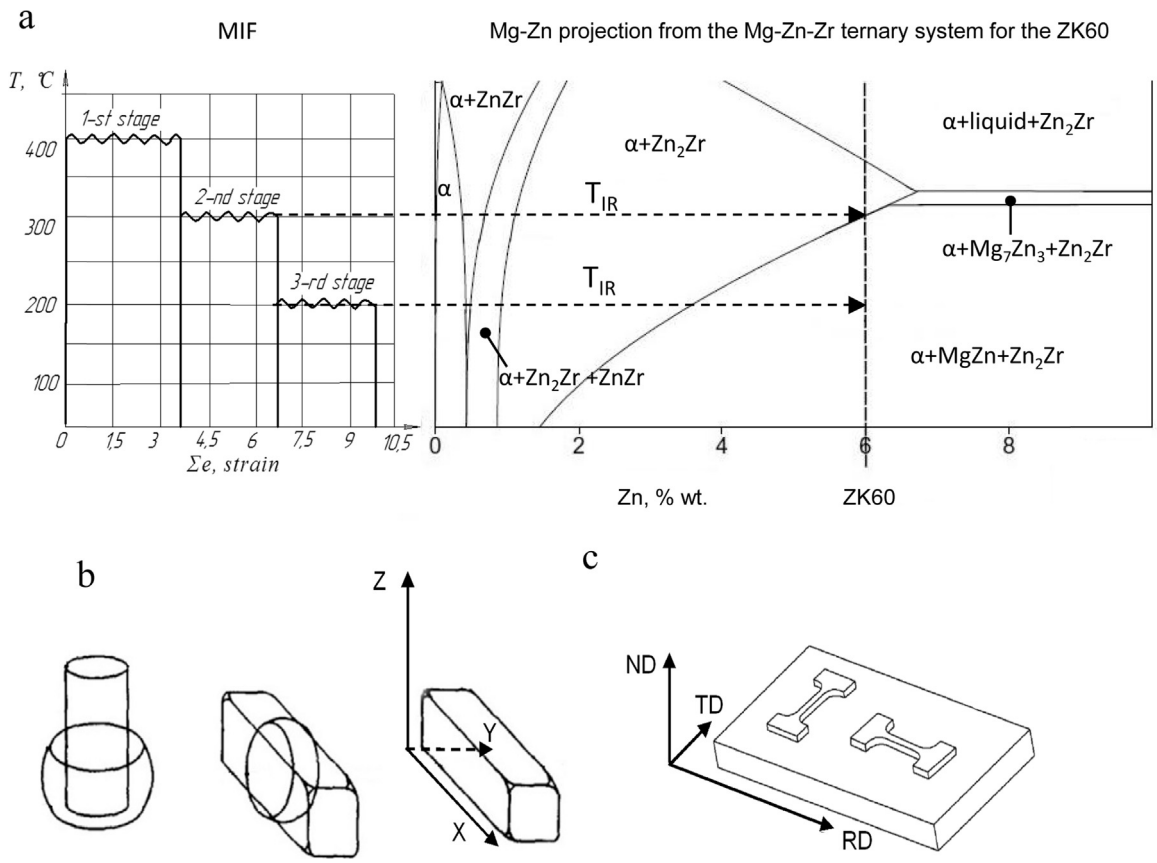

Fig. 1. (a) True strain-temperature stages during multi-step isothermal forging (MIF) of ZK60 and the link to the Mg-Zn phase diagram. Schematics of: (b) MIF and (c) isothermal rolling (IR).

reductions corresponding to true strains of 0.51, 0.91, and 1.6.

2.2. Material characterization and mechanical testing

The alloy microstructure and texture were characterized in the longitudinal plane (X-Z or RD-ND) and transverse plane (Y-Z or TD-ND) by transmission electron microscopy (TEM) in an JEOL-2000EX and scanning electron microscopy (SEM) using backscatter electrons (BSE) and electron backscattered diffraction (EBSD) in a Tescan Mira LM SEM equipped with an HKL CHANNEL 5 software. For metallographic examination and subsequent SEM-based EBSD measurements, the samples were mechanically polished using standard methods and electro-polished in 5 ml nitric acid and 95 ml methanol solution under the 20 V during 20–30 s at −5 °C. Thin foils for TEM investigations were prepared by subsequent mechanical polishing and final electro-polishing in a 50 ml nitric acid, 100 ml glycerin, and 850 ml methanol solution under 15 V at $-5 \pm (-1)$ °C using Tenupol 5.1 equipment.

The sizes of the sub-grains and grains (d_{subg} and d_g) (surrounded by low- and high-angle boundaries with $\theta \geq 2$ and 15°, respectively) were estimated from EBSD maps employing the linear intercept method and following the equivalent diameter method. Grain size was also measured by means of optical microscopy (OM) using linear intercept method. The volume fractions and sizes of other structural components were determined in BSE SEM images and TEM images by the point-count method and direct measurements.

Analysis of excess phase particles as well as the second-phase precipitates (β' - phase and zirconium dispersoids Zn_2Zr) of a size of < 500 nm was performed employing the software package ImageJ2x, using images of the material in two orthogonal planes before and after IR. Depending on the precipitate density and size, five to eight images were used to collect statistically significant information. The area fraction measurement, S_β, per image included at least 5000 precipitates. Since the β' precipitates are disk-shaped, we estimated three quantities to describe their size: the average value of the maximum diameter L_p, minimum diameter T_p and average equivalent diameter D_p (diameter of the circle corresponding to the area equal to the particle section area). Finally, the average distance between the precipitates, λ, was estimated from D_p and S_β using [53]:

$$\lambda = D_p \sqrt{\frac{\pi}{6S_\beta}}. \quad (1)$$

Particle strengthening was calculated using Orowan's formula, which relates the stress required to bow dislocations around the particles with the interparticle spacing λ:

$$\Delta\tau = \frac{Gb}{2\pi\sqrt{(1-\nu)}} \frac{1}{\lambda} log\left(\frac{D_p}{r_0}\right), \quad (2)$$

where $\Delta\tau$ is the increase in slip resistance due to precipitate strengthening, $G = 20.2$ GPa is the shear modulus of the Mg–Zn solid solution, $b = 3.2 \times 10^{-10}$ m is the magnitude of the Burgers vector of the a-dislocation in Mg [1,23], ν is the Poisson's ratio taken to be 0.33, λ is the effective interparticle spacing on the slip plane, and r_0 is the dislocation core radius equal to Burgers vector value.

In addition, pole figures were measured using an X-ray diffractometer (XRD) with a Rigaku Ultima IV goniometer, which relies on Bragg-Brentano method for an automatic pole figure measurements. Measured pole figures were in the RD-TD plane. Incomplete pole figures were measured using Cu K_α- radiation (45 kV, 30 mA), reflected from a flat graphite monochromator < 0002 > . The radial angle γ ranged from 0° to 75°, and the azimuth angle δ from 0° to 360°. The wavelengths used were $K_{\alpha1}$ = 1.54060 Å and $K_{\alpha2}$ = 1.54439 Å. Orientation distribution functions (ODF) corresponding to the measured pole figures were calculated using the Matlab program MTex 4.2.1.

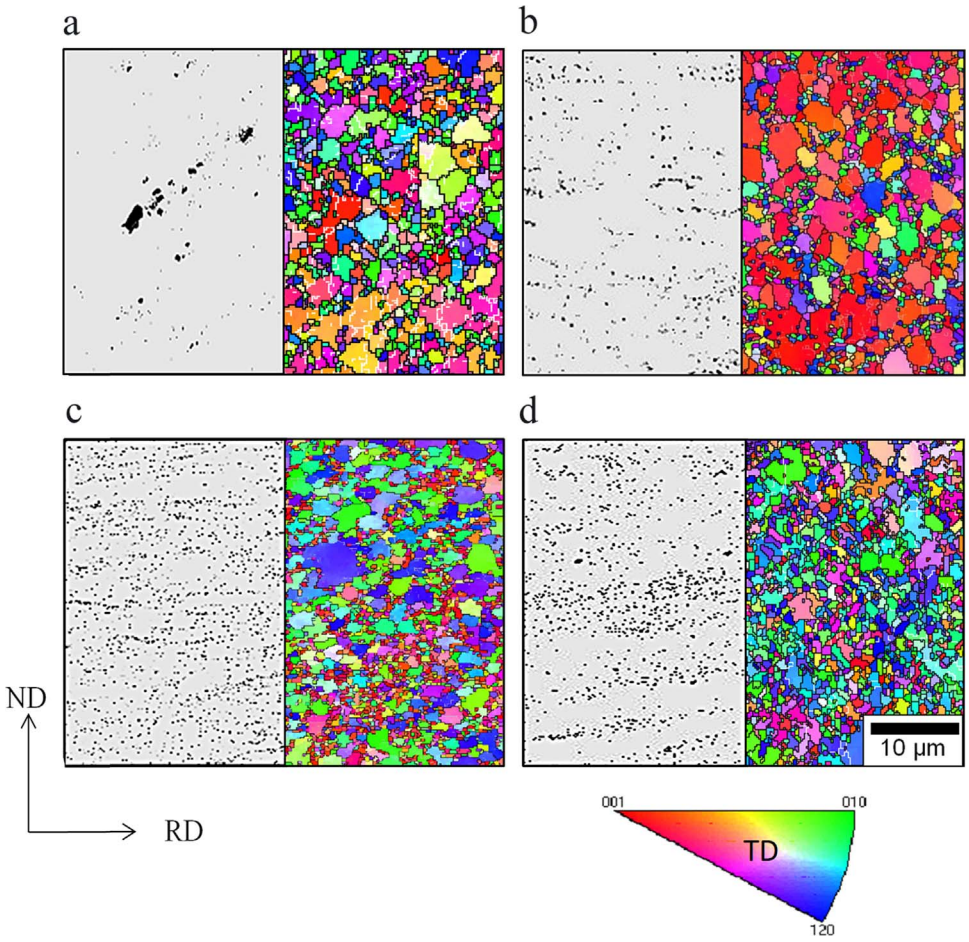

Fig. 2. BSE image (left) and EBSD maps (right) of ZK60 alloy: (a) after MIF and after IR to true strains of (b) 0.51, (c) 0.91 and (d) 1.6 at 200 °C.

Tensile tests were carried out at room temperature on the Instron 5982 using flat samples with a 10 × 2 × 2 mm gage, cut from the initial rod, MIF billet and IF rolled sheets with orientations indicated in Fig. 1c.

3. Experimental results

3.1. Grain structure and texture

The FG and UFG structures formed after the MIF process consists of approximately 90% homogeneous recrystallized grains. Typical orientation image maps of ZK60 before and after IR to true strains of 0.51, 0.91 and 1.6 at 200 °C in ND-RD plane are presented the Fig. 2. The grain structure before IR features recrystallized (sub)grains size of (0.9) 3 (by EBSD equivalent diameters method, 4.5 by OM) μm (Fig. 2a). The grain structure undergoes a slight grain refinement during IR to approximately (0.8) 2 (3.5 by OM) μm (Fig. 2d). In spite of the high rolling strain $e = 1.6$ most of grains are equiaxed (Fig. 2d), a likely result of dynamic recrystallization. A fraction of non-recrystallized large grains (~ 10%) that had fragmented along the elongation direction was also observed. Table 1 summarizes the estimated average (sub) grain sizes and total twin volume fractions. The fraction of boundaries corresponding to the twin/parent grain relationship, V_{twin}, was estimated after the tension tests and no significant increase was found. For example, the MIF sample before tension was characterized with 21% of twin boundaries and after tension, this value increased only to 24%. The fraction of high angle grain boundaries, V_{HAB}, was estimated after MIF and after each of the subsequent IR steps. The measurements show that V_{HAB} was large after MIF (75%) and increased further after the second IR step.

Table 1
Microstructural parameters in the processed samples at 200 °C. The grain size values were determined by equivalent diameter method in HKL software.

Sample	d_g [μm]	d_{subg} [μm]	V_{HAB}, [%]	V_{twin}, [%]
MIF	3	0.9	75	21
MIF + IR, $e = 0.51$	2	0.8	83	23
MIF + IR, $e = 0.91$	2	0.8	88	25
MIF + IR, $e = 1.60$	1.2	0.8	87	24

Fig. 3 shows the corresponding texture measured by XRD. The analysis indicates that the grains reoriented during the IR process from the deformation texture produced after the MIF to form a strong basal texture {0001} that strengthens with rolling strain.

MIF at 200 °C led to the formation of a preferred texture with a maximum located at $\{10\bar{1}2\} < 0\ \bar{1}\ 10 >$ and a weak peak at {0001} (Fig. 3a). After rolling to $e = 0.51$, the texture weakened with most of the planes {0001} lying within ~ (20°) from the ND (Fig. 3b). After IR to $e = 0.91$ the original texture has completely transformed (Fig. 3c) and eventually after a strain to 1.6 became a predominant basal texture (Fig. 3d). Evidently, the texture and grain sizes are very similar upon IR, and as a result these are not expected to govern any potential plastic anisotropy exhibited by the material.

3.2. Second phases

Fig. 2a shows that forged material contains a high fraction of coarse (up to a few micrometers in size) particles of excess phases (predominantly near-equilibrium Mg-Zn eutectic phases) aligned in the form of strings. It is observed that rolling changed the appearance of

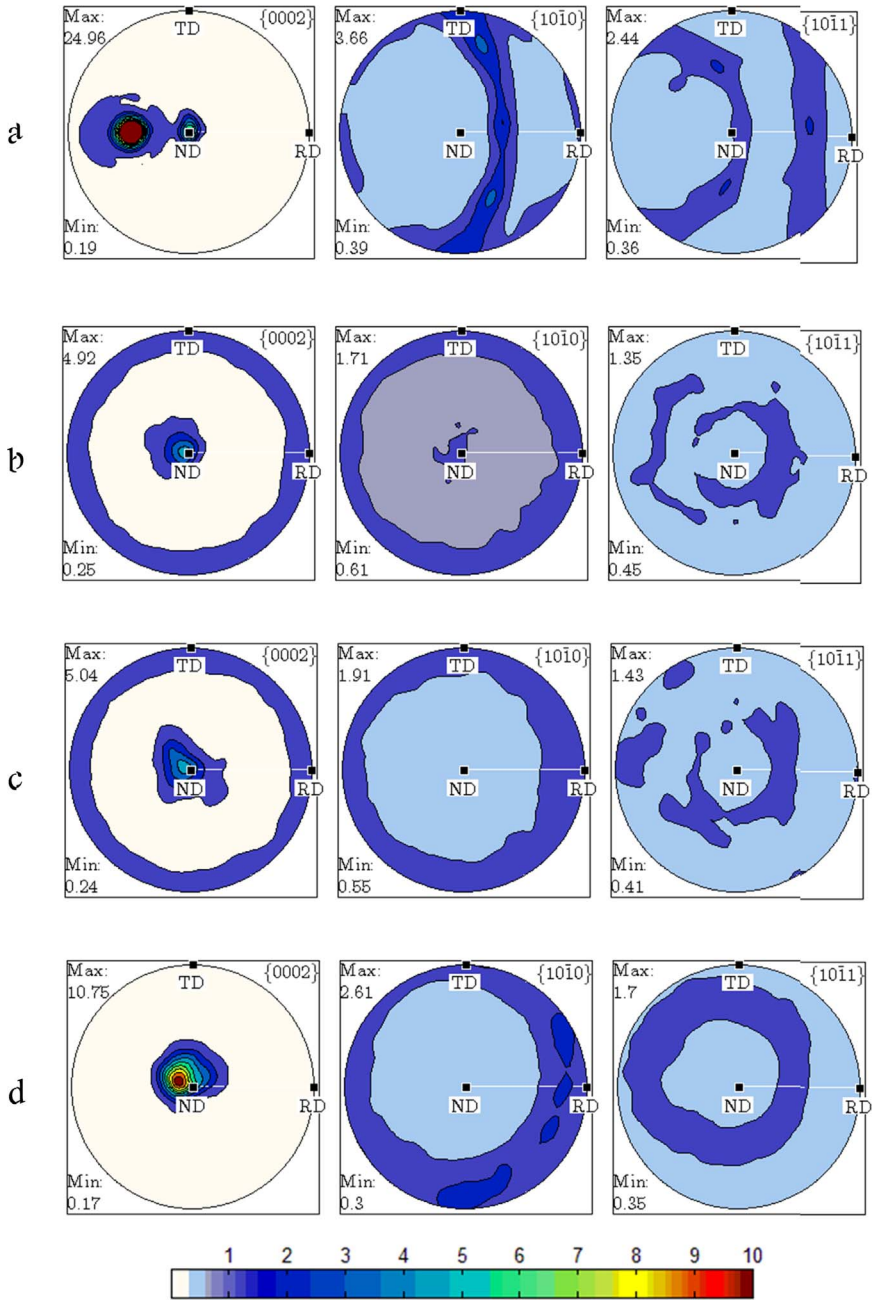

Fig. 3. Pole figure measured by X-ray diffraction (XRD) showing texture in the ZK60 alloy: (a) before and after IR to true strain levels of (b) 0.51, (c) 0.91, and (d) 1.6 at 200 °C.

these phases significantly. Firstly, the particles refined considerably and the strings became less evident with increasing IR strain, as shown in Fig. 2b. Eventually after some amount of strain, the IR process resulted in the reappearance of the string-type particle arrangement, similar to that in the initial state, but with notably shorter, narrower and closer spaced strings comprised of smaller particles, Fig. 2c.

BSE and TEM analyses show that, in addition to the coarse excess phases, dispersed secondary phases of the order of < 500 nm in size are present in all samples. These precipitates were identified as Zn_2Zr and Mg-Zn β'-type phases, which are commonly observed in aged ZK-type Mg-Zn alloys with Zr additions [1,6,17]. Fig. 4 shows representative TEM and BSE images of these precipitates in the ND–RD plane. During deformation at the temperature of single-phase region (see Mg-Zn phase diagram in Fig. 1a) fine particles are mainly stable precipitates Zn_2Zr, which do not significantly change with MIF and IR at 300 °C. In contrast, during processing at 200 °C (i.e. at the temperature of two-phase region (see Fig. 1a)), additional precipitates form. The size and volume fraction of these precipitates increase with time and strain under the precipitation deformation conditions due to the decomposition of the magnesium solid solution (Fig. 4d-f). Moreover, the second phase particles could split and coagulation due to severe mechanical straining [52].

In an effort to further characterize any other changes in microstructure during processing of the material, we measure the area fraction and geometry of second-phase particles. The data are based on examining multiple BSE micrographs per sample at the specific deformation state and plane. The measured and calculated values are presented in Table 2.

It is seen from Table 2 that the average precipitate geometry, as well as their mean area fractions, in both longitudinal and transverse sections of the billets and sheets processed to the three strain levels at 300 °C are similar. The main reason is prevailing number of small stable precipitates over the "unstable" large particles, which outweighs the effect of refining of the latter at this temperature. In contrast, the

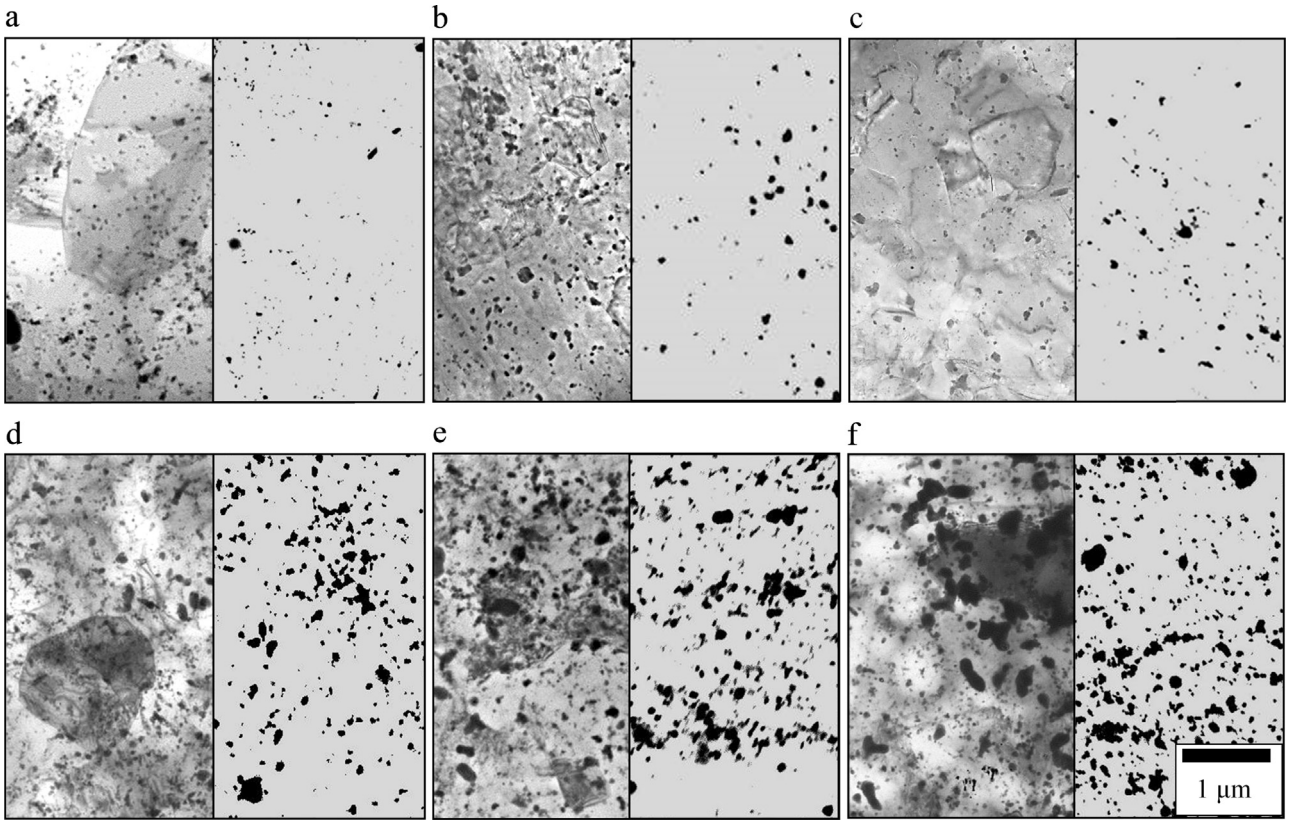

Fig. 4. TEM (left) and BSE (right) images showing particles in the ZK60 alloy after MIF (a, d) and after IR to true strain levels of 0.91(b, e) and 1.6 (c, f) at 300 (a-c) and 200 °C (d-f).

Table 2
Second-phase particles (precipitates) in the alloy structure in longitudinal (RD-ND) section/transverse (TD-ND) section: area fraction, S_β, average value of maximal diameter, L_p, average value of minimal diameter, T_p, average equivalent diameter D_p, and the average distance between the precipitates, λ. Δτ is the estimated increase in slip resistance due to precipitate strengthening using Eq. (2).

Sample		S_β [%]	L_p [nm]	T_p [nm]	λ [nm]	D_p [nm]	Δτ [MPa]
300C	MIF	3.4/3.3	65/85	40	230/270	60/65	4.89/5.75
	IR 0.91	3.4/4.0	90/75	50	265/225	65/60	6.20/6.01
	IR 1.60	3.3/3.9	85/80	50	270/240	70/65	5.75/6.06
200C	MIF	5.8/6.5	70/85	55	220/240	75/85	5.65/6.47
	IR 0.91	11.1/10.6	110/75	30	170/130	80/60	11.53/ 10.41
	IR 1.60	15.4/13.0	130/55	20	165/75	90/35	13.49/ 11.47

deformation at 200 °C under the conditions of decomposition of the solid solution leads to the formation of new disperse phases with dimensions up to 50 nm [54]. The evolution of precipitate geometry with plastic strain is found to be anisotropic.

Note that second-phase particles were measured to be of near-spherical shape after MIF at both 300 °C and 200 °C (Table 2). In contrast, IR at 200 °C led to significant difference in D_p between transverse and longitudinal cross sections. Moreover, the particle average lengths and spacing are noticeably different for IR to a strain of 1.6 at the 200 °C. In particular, new precipitates are found much smaller in the transverse plane than in the longitudinal plane. These findings suggest that in addition to the temperature conditions of the deformation, another important factor affects the decomposition of the solid solution like the changing structure of the alloy matrix. Structural parameters, such as the (sub)grain size, were not found to affect significantly the secondary phase precipitation in this alloy, since the main decomposition of solid solution during both forging and rolling occurred in a uniform, highly refined, and almost recrystallized structure. However, the effect of the crystallographic texture under dynamic aging conditions appears to be much more significant [52,54].

The decomposition of the Mg-Zn solution began statically as the billet was heated up to 200 °C in the last MIF stage and then proceeded dynamically directly during the forging process, resulting in a textured matrix (Fig. 3a). At this stage in processing of the alloy, only a small fraction of the dispersed β'-type phase precipitated, in addition to the existing second phases (Table 1). As mentioned above, the fine secondary β'-type phase precipitates in ZK60 are rod (β_1')- or disk (β_2')-shaped [35,55]. They appear upon static aging to be strongly orientation-dependent and form predominantly along prismatic or basal planes in the hexagonal-close packed magnesium lattice structure, respectively [27,28,55,56]. According to [55], the precipitate-matrix orientation relationships are: $(11\ \bar{2}\ 0)_{\beta1'}||(0001)_{Mg}$, $[0001]_{\beta1'}||[11\ \bar{2}\ 0]_{Mg}$ between β_1' and Mg and $(0001)_{\beta2'}||(0001)_{Mg}$, $[11\ \bar{2}\ 0]_{\beta2'}||[1010]_{Mg}$ between β_2' and Mg. However, the directions of the precipitates during dynamic aging under MIF in Mg-Zn-Zr alloys can be different from that in static aging because of multiple deformation path changes and severe straining. Therefore, the products of the solid solution decomposition were randomly distributed in the forged billet and had a little effect on the phase parameters presented in Table 2.

Both static and dynamic aging continued with heating and IR at 200 °C. In this case, a significant fraction of the hardening phase was precipitated, simultaneously with the progressive strain-induced lattice rotation and formation of a strong rolling texture (see Fig. 3b-d). The aging conditions during unidirectional rolling along with more uniform straining during IR than MIF altered the precipitate growth [27,28]. As a result of the preferred formation of texture and simultaneous precipitation and growth of new oriented β' - phase particles along with the already existing precipitates led to the preferential orientation of the precipitates. The average thickness and length of all the second phases decreased in the transverse section, while these increased in the longitudinal section with straining (Table 2). The ratio of interparticle distances along and across the axis of sheets rolled to the true strain of 1.6

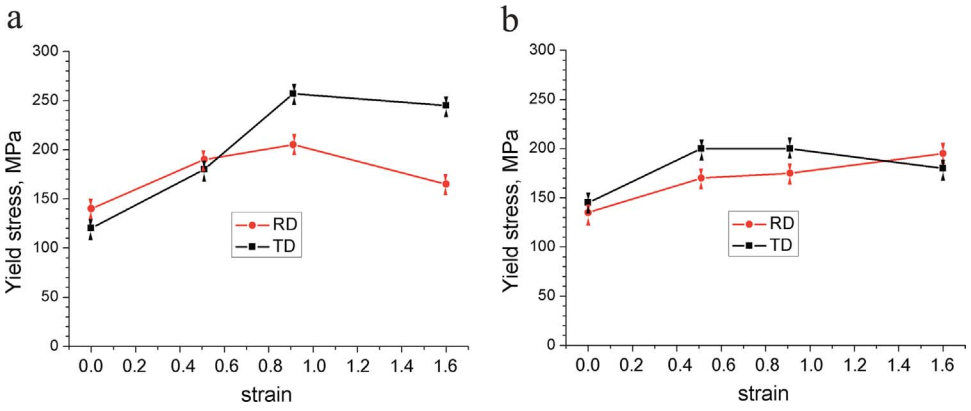

Fig. 5. Yield stress measured on the samples after IR at (a) 200 °C and (b) and 300 °C along the rolling direction (RD) and the transverse direction (TD).

exceeds 2.

In summary, rolling at a temperature below the solvus leads to a very anisotropic formation of the second phases due to the texture-controlled decomposition of magnesium solid solution during dynamic aging. This could be the main cause for the yield strength anisotropy in a rolled ultrafine-grained alloy under tension at room temperature, as will be studied below. In contrast, during the IR at 300 °C strings of second phases develop with no significant anisotropy in their distribution.

3.3. Tensile yield stress

The tensile yield stress for the IR samples studied here as a function of the accumulated strain is given in Fig. 5. It is seen that IR at the (a) 200 °C and (b) 300 °C resulted in appreciable strengthening in the rolling direction (RD) as indicated by the increase in yield stress (YS). Significantly we observe yield stress increases ranging from 140 to 190 MPa after rolling to a strain of $e = 0.91$ at the 200 °C (Fig. 5a) and similarly after rolling to a strain of 1.60 at the 300 °C (Fig. 5b). Most remarkable is the anisotropic strengthening to 260 MPa and 245 MPa in the transverse direction after rolling strain to strains of $e = 0.91$ and $e = 1.6$ at the 200 °C, respectively. As a result, the alloy mechanical response became more anisotropic in YS after rolling at the 200 °C but significantly less anisotropic in YS after rolling at the 300 °C. The reason for this difference must lie in an outstanding difference in their microstructure as a result of the 200 °C versus 300 °C processing. In the next sections, we use polycrystal modeling calculations via EPSC to help give insight into the origin of this difference.

4. Modeling framework

4.1. Summary of EPSC model

In this work, we employ the polycrystal EPSC model [57] to calculate stresses and strains in the microstructure during deformation. As all polycrystal models of its class, it is used to relate the response of an aggregate to that of each of its single crystals. Each crystal is modeled as an ellipsoidal inclusion in a homogeneous effective medium (HEM) with a specific orientation and volume fraction. The properties of the HEM are equal to the properties of the polycrystal and are calculated by enforcing that the polycrystal stress and strain equals the average stress and strain of all its constituent crystals.

In this section, the EPSC model is reviewed. The expressions follow the conventional notation in that we use "·" to denote a contracted or dot product and "⊗" for an uncontracted or tensor dyadic product.

The macroscopic Jaumann stress rate and strain rate are related by the following linear relationship:

$$\hat{\boldsymbol{\sigma}} = \mathbf{L}\dot{\boldsymbol{\varepsilon}}, \tag{3}$$

where $\mathbf{L}$ is the instantaneous elasto-plastic stiffness tensor of the polycrystal. A self-consistent procedure [57] is used to solved for $\mathbf{L}$, iteratively [58]. Likewise, for a given grain (or inclusion) the local strain increment and the macroscopic strain increment are related by:

$$\dot{\boldsymbol{\varepsilon}}^c = \mathbf{A}^c\dot{\boldsymbol{\varepsilon}}, \tag{4}$$

where $\mathbf{A}^c = (\mathbf{L}^c + \mathbf{L}^{c,*})^{-1}(\mathbf{L}+\mathbf{L}^{c,*})$ is the localization tensor for inclusion and $\mathbf{L}^c$ is the instantaneous elasto-plastic stiffness tensor for crystal, c. The effective stiffness is given by

$$\mathbf{L}^{c,*} = \mathbf{L}(\mathbf{S}^{c-1} - \mathbf{I}) \tag{5}$$

and is used in the following interaction equation:

$$(\hat{\boldsymbol{\sigma}}^c - \hat{\boldsymbol{\sigma}}) = -\mathbf{L}^{c,*}(\dot{\boldsymbol{\varepsilon}}^c - \dot{\boldsymbol{\varepsilon}}), \tag{6}$$

to relate the Jaumann stress rate deviation and total strain rate deviation from macroscopic value in crystal c. In Eq. (5), $\mathbf{S}^c$ is the symmetric Eshelby tensor and $\mathbf{I}$ is the fourth rank identity matrix. By enforcing that the macroscopic Jaumann stress rate and strain rate are equal to the volume average of the grain Jaumann stress rate and strain rate, i.e.,

$$\hat{\boldsymbol{\sigma}} = \langle\hat{\boldsymbol{\sigma}}^c\rangle, \tag{7}$$

and

$$\dot{\boldsymbol{\varepsilon}} = \langle\dot{\boldsymbol{\varepsilon}}^c\rangle, \tag{8}$$

we obtain an expression the following expression for the macroscopic stiffness $\mathbf{L}$:

$$\mathbf{L} = \langle\mathbf{L}^c\mathbf{A}^c\rangle\langle\mathbf{A}^c\rangle^{-1}. \tag{9}$$

For a given crystal c, the constitutive relationship between its $\hat{\boldsymbol{\sigma}}^c$ and $\dot{\boldsymbol{\varepsilon}}^c$ is:

$$\hat{\boldsymbol{\sigma}}^c = \mathbf{C}^c\left(\dot{\boldsymbol{\varepsilon}}^c - \sum_s \mathbf{m}^{c,s}\dot{\gamma}^{c,s}\right) - \sigma^c tr(\dot{\boldsymbol{\varepsilon}}^c), \tag{10}$$

where $\mathbf{C}^c$ is the elastic stiffness tensor for crystal c. The plastic strain rate is given by the sum of plastic shear strain rates over all slip systems $\sum_s \mathbf{m}^{c,s}\dot{\gamma}^{c,s}$; where $0.5(\mathbf{b}^{c,s} \otimes \mathbf{n}^{c,s} + \mathbf{n}^{c,s} \otimes \mathbf{b}^{c,s})$ is the Schmid tensor for slip system s; and $\mathbf{b}^{c,s}$ and $\mathbf{n}^{c,s}$ are the unit vectors for the slip direction and slip plane normal, respectively. In the calculation, $\mathbf{C}^c$ is updated at the beginning of each deformation increment and takes into account texture changes. For Mg, the invariant elastic single crystal constants are: $C_{11} = 59.4GPa$, $C_{33} = 61.6GPa$, $C_{12} = 25.6GPa$, $C_{13} = 21.4GPa$, $C_{44} = 16.4GPa$ and $C_{66} = 16.9GPa$ [59].

Two criteria are employed to activate a slip system: (1) $\boldsymbol{\sigma}^c\cdot\mathbf{m}^s = \tau^s$, meaning that the resolved shear stress needs to reach the slip resistance, τ^s and (2) $\hat{\boldsymbol{\sigma}}^c\cdot\mathbf{m}^s = \dot{\tau}^s$, which signifies that the stress must remain on the single crystal yield surface. Since these criteria do not allow for negative shear on any given slip system, each slip system is divided into two slip systems having the same plane normal but opposite sense of shearing.

The rate of slip resistance, $\dot{\tau}^s$, is related to the shear rate, via $\dot{\gamma}^{s'}$:

$$\dot{\tau}^s = \sum_{s'} h^{ss'}\dot{\gamma}^{s'}, \tag{11}$$

where $h^{ss'}$ is the hardening matrix. The $h^{ss'}$ used here can be found in prior works [60,61].

Finally, the crystal stress increment and strain increment are linearly related by the following:

$$\hat{\boldsymbol{\sigma}}^c = \mathbf{L}^c\dot{\boldsymbol{\varepsilon}}^c, \tag{12}$$

where $\mathbf{L}^c$ is:

$$\mathbf{L}^c = \mathbf{C}^c - \mathbf{C}^c\sum_s \mathbf{m}^s \otimes \left(\sum_{s'}\left(X^{ss'}\right)^{-1}\mathbf{m}^{s'}(\mathbf{C}^c - \boldsymbol{\sigma}^c \otimes \mathbf{i})\right) - \boldsymbol{\sigma}^c \otimes \mathbf{i}, \tag{13}$$

with:

$$X^{ss'} = h^{ss'} + \mathbf{C}^c\bullet\mathbf{m}^s \otimes \mathbf{m}^{s'}. \tag{14}$$

The rotations of crystals are taken into account by applying the elastic spin rate $\mathbf{W}^c$ to rotate single crystals. The elastic spin rate is calculated as:

$$\mathbf{W}^c = \mathbf{W}^{app} + \boldsymbol{\Pi}^c - \mathbf{W}^{pl,c}, \tag{15}$$

with:

$$\mathbf{W}^{pl,c} = \sum_s \dot{\gamma}^s\,\mathbf{q}^s \tag{16}$$

$$\boldsymbol{\Pi}^c = \mathbf{P}^c(\mathbf{S}^c)^{-1}(\dot{\boldsymbol{\varepsilon}}^c - \dot{\boldsymbol{\varepsilon}}) \tag{17}$$

where $\mathbf{W}^{app}$ is macroscopically applied spin rate, $\boldsymbol{\Pi}^c$ is the spin rate of crystal c due to applied macroscopic strain rate on HEM, $\mathbf{P}^c$ is the antisymmetric Eshelby tensor, $\mathbf{W}^{pl,c}$ is plastic spin, $\mathbf{q}^s = \frac{1}{2}(\mathbf{b}^s \otimes \mathbf{n}^s - \mathbf{n}^s \otimes \mathbf{b}^s)$ is antisymmetric shcmid tensor.

4.2. Hardening law

In the current version of the EPSC model, the CRSS for each slip system to activate depends on the evolution of stored dislocations. Here we review the evolution equations for the CRSS on each system. Details on the model can be found in prior works [62,63].

In the model, the CRSS for slip system s or the resistance to slip τ_c^s, is given by

$$\tau_c^s = \tau_{o,f}^s + \tau_{0,HP}^s + \tau_{for}^s + \tau_{sub}^s. \tag{18}$$

where $\tau_{o,f}^s$ is a friction stress, which does not evolve with strain, and that depends on present precipitates, $\tau_{0,HP}^s$ is grain size dependent term, and τ_{for}^s and τ_{sub}^s are the resistances due to the storage of forest and substructure and these evolve with strain.

The Hall-Petch effect term is given by:

$$\tau_{HP}^s = \mu^\alpha HP^\alpha\sqrt{\frac{b^\alpha}{d_g}} \tag{19}$$

where HP^s is the Hall-Petch parameter, μ^α is the effective shear modulus for each slip mode, α, b^α, is the magnitude of the Burgers vector and d_g is the grain size. For basal, prismatic, and pyramidal slip modes the Burgers vectors are 3.21×10^{-10} m, 3.21×10^{-10} m, and 6.12×10^{-10} m, respectively. This term is modified when twins are present, to include the spacing d_{mfp} between adjacent twin boundaries, i.e. [48,60],

$$\tau_{0,HP}^s = \mu^s HP^s\sqrt{\frac{b^s}{d_{mfp}}}. \tag{20}$$

The evolution of τ_{for}^s is dependent on the evolution of the spatially random distribution of stored dislocations and is related to the stored forest dislocation density ρ_{for}^s by

$$\tau_{for}^s = b^\alpha\chi\mu^\alpha\sqrt{\sum_{s'} L^{ss'}\rho_{for}^{ss'}} \tag{21}$$

where χ^s is a dislocation interaction parameter of order unity. In this study, we set it to 0.9 for each slip system, s and do not treat it as a fitting parameter.

The τ_{sub}^s is the stored dislocations in the substructure and related to the substructure density ρ_{sub}^s via:

$$\tau_{deb}^\alpha = k_{deb}\mu^\alpha b^\alpha\sqrt{\rho_{deb}}\,log\left(\frac{1}{b^\alpha\sqrt{\rho_{deb}}}\right). \tag{22}$$

where $k_{sub} = 0.086$ is a mathematical constant. For an annealed material, the initial dislocation density can be approximately $1.0^{12}\,\mathrm{m}^{-2}$ for ρ_{for}^s and $0.1\,\mathrm{m}^{-2}$ for ρ_{sub}^s.

The forest density ρ_{for}^s evolves according to [64–66]:

$$\frac{\partial\rho_{for}^s}{\partial\gamma^s} = k_1^\alpha\sqrt{\rho_{for}^s} - k_2^\alpha(\dot{\varepsilon}, T)\rho_{for}^s, \tag{23}$$

where k_1^α is the rate coefficient for the rate of statistical trapping of glide dislocations by forest obstacles, and γ^s is the shear strain. It represents a balance between the rate of dislocation generation (or storage), $\frac{\rho_{gen,for}^s}{\gamma^s}$, and the rate of dislocation removal, $\frac{\rho_{rem,for}^s}{\gamma^s}$. The coefficient k_2^s is the rate coefficient for dynamic recovery and is expressed by:

$$\frac{k_2^\alpha}{k_1^\alpha} = \frac{\chi b^\alpha}{g^\alpha}\left(1 - \frac{k_B T}{D^\alpha(b^\alpha)^3}ln\left(\frac{\dot{\varepsilon}}{\dot{\varepsilon}_0}\right)\right) \tag{24}$$

where k, $\dot{\varepsilon}$, $\dot{\varepsilon}_0 = 1 \bullet 10^7$, g^α and D^α are, respectively, the Boltzmann constant, the applied strain rate, a reference strain rate, an effective activation enthalpy and a drag stress.

The activation stress, τ_c^t, of the twin system is given by:

$$\tau_c^t = \tau_0^\beta + \tau_{0,HP}^t + \mu^\beta\sum_s C^{\beta\alpha}(\dot{\varepsilon})b^\beta b^\alpha\rho_{for}^s \tag{25}$$

where τ_0^β is a friction term, and $\tau_{o,HP}^t$ is a Hall-Petch term for the effect on grain size. The latter term is affected by d_g according to:

$$\tau_{HP}^t = \mu^\beta HP^\beta\sqrt{\frac{b^\beta}{d_g}} \tag{26}$$

However when twins are present, d_g changes to d_{mfp} [48,60]:

$$\tau_{HP}^t = \mu^\beta HP^\beta\sqrt{\frac{b^\beta}{d_{mfp}^t}}. \tag{27}$$

The final term represents the effects of latent hardening by the activity of slip on the twin system. It includes the product of the value of the Burgers vectors of the slip and twinning dislocations, where the Burgers vector for the $\{10\bar{1}2\}$ twin is 0.247×10^{-10} m. The new twin is assigned appropriate orientation so that it satisfies orientational relationship with its parent. The new twins are treated as separate grains [60]. The initial stress and strain state within the twins are assigned using the finite initial fraction (FIF) assumption [67].

4.3. Type I and II residual stress determination using EPSC modeling framework

Residual stress types are defined based on the length scale over which they self-equilibrate: the component scale (type I), grain scale (type II) and atomic scale (type III) [68]. The superposition of these three stress fields gives the true residual stress present in the material. The effect of the true superposed stress field on the inter-planar spacing is measured by X-ray diffraction. The source of the residual stress at all length scales is inhomogeneous plastic deformation. To evaluate the residual stresses at the end of MIF + IR with $e = 1.6$, we employ a method for estimating type I and II residual stresses based on the measured inter-planar spacing by X-ray diffraction proposed for cubic materials [69,70] and recently extended to hexagonal materials [71,72].

The total elastic strain of the diffracting grain in the direction

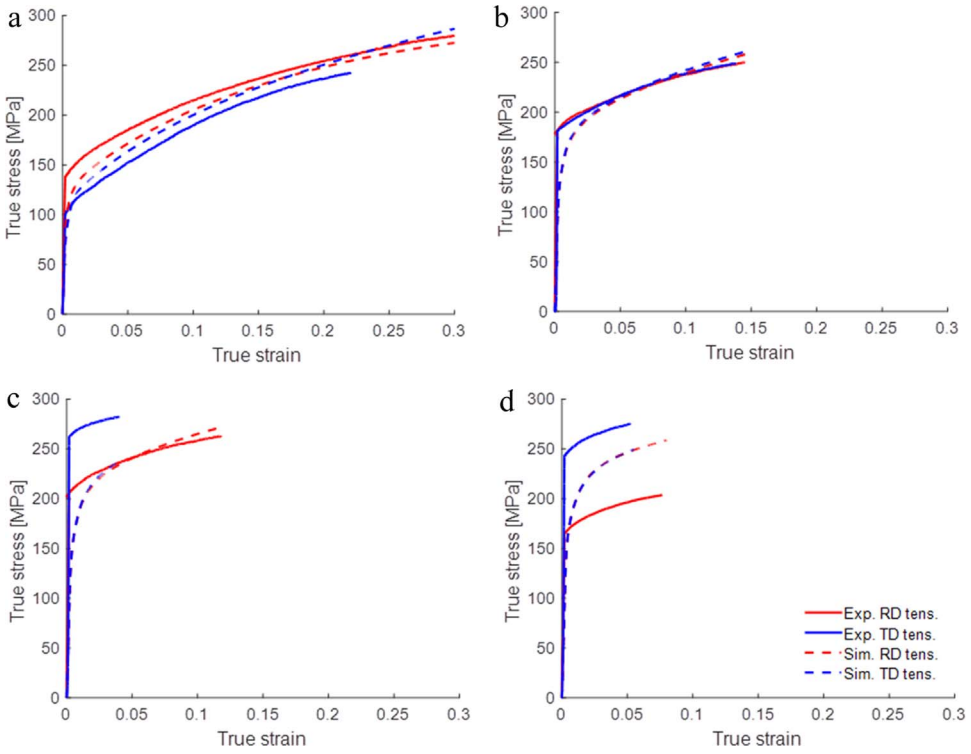

Fig. 6. Flow curves of the material (a) before and (b-d) after IR to true strains of (b) 0.51, (c) 0.91 and (d) 1.6.

determined by the scattering vector is the superposition of elastic strains coming from two residual stress fields as follows:

$$\varepsilon^{c}(\Phi, \Psi, hkil) = \varepsilon^{I,c}(\Phi, \Psi, hkil) + \varepsilon^{II,c}(\Phi, \Psi, hkil) \tag{28}$$

where $\varepsilon^{I,c}(\Phi, \Psi)$ is normal elastic strain in the direction of the scattering vector as a function of angles Φ and Ψ corresponding to the type I residual stress and $\varepsilon^{II,c}(\Phi, \Psi)$ is the elastic strain associated with the type II residual stress. The angle $\Phi = 0°$ is measured between RD and projection of scattering vector to RD-TD plane, while the angle $\Psi = [7.5°15°20°25°30°35°40°45°50°55°60°]$ is measured between ND and scattering vector.

After performing the volume average over diffracting grains and with some additional manipulations, the relation (25) becomes [71]:

$$\langle\varepsilon^{c}(\Phi, \Psi, hkil)\rangle = F_{ij}(\Phi, \Psi, hkil)\sigma_{ij}^{I} + \langle\varepsilon^{II,c}(\Phi, \Psi, hkil)\rangle \tag{29}$$

where $F_{ij}(\Phi, \Psi, hkil)$ are diffraction elastic constants and σ_{ij}^{I} is the type I residual stress. Diffraction elastic constants can be evaluated for given texture and single crystal elastic constants using the following expression:

$$F_{ij}(\Phi, \Psi, hkil) = \langle n_p(\Phi, \Psi) n_q(\Phi, \Psi) A_{pqkl}^{c}\rangle S_{klij} \tag{30}$$

where n_p is the scattering vector, A_{pqkl}^{c} is the localization tensor for crystal c and S_{klij} is the elastic compliance tensor of polycrystal. The EPSC model can provide values for the last two tensors.

The elastic strain coming from the type II residual stress is approximated by:

$$\langle\varepsilon^{II,c}(\Phi, \Psi, hkil)\rangle = q\langle\varepsilon^{II,c,pred}(\Phi, \Psi, hkil)\rangle \tag{31}$$

where q is a scaling factor and $\langle\varepsilon^{II,c,pred}(\Phi, \Psi, hkil)\rangle$ is the EPSC predicted value for the elastic strain due to the applied deformation. The scaling factor q needs to be introduced since we presume that EPSC can predict the dependence of the type II residual stress with grain orientation, but not its absolute value.

The value accessible by X-ray diffraction is the inter-planar spacing $d_{hkil}(\Phi, \Psi)$ of the *hkil* plane perpendicular to the scattering vector and is related to the average elastic strain of the diffracting grains in the direction of the scattering vector via the following relation:

$$d_{hkil}(\Phi, \Psi) = [F_{ij}(\Phi, \Psi, hkil)\sigma_{ij}^{I} + q\langle\varepsilon^{II,c,pred}(\Phi, \Psi, hkil)\rangle]d_{hkil,0} + d_{hkil,0} \tag{32}$$

where $d_{hkil,0}$ is the inter-planar spacing of the stress-free material. The values of σ_{ij}^{I}, q and $d_{hkil,0}$ are determined as fitting parameters using the least square method and assuming a biaxial stress state [70]:

$$\sigma_{ij}^{I} = \begin{bmatrix} \sigma_{11}^{I} & 0 & 0 \\ 0 & \sigma_{22}^{I} & 0 \\ 0 & 0 & 0 \end{bmatrix}. \tag{33}$$

The least square fitting is to be performed with lower and upper bounds on fitting parameters σ_{11}^{I}, σ_{22}^{I}, q and $d_{hkil,0}$, so that they retain reasonable values. The bounds are necessary mostly for macroscopic stress σ_{22}^{I}, since the fitting algorithm has tendency to overpredict this stress due to the fact that we are using only one data set with different values of angle Ψ but only one value of angle $\Phi = 0°$. Therefore the stress direction is perpendicular to the direction in which $\varepsilon^{I,c}(\Phi, \Psi, hkil)$ strain is measured. Due to perpendicularity between σ_{22}^{I} and $\varepsilon^{I,c}(\Phi, \Psi, hkil)$ direction the effect of σ_{22}^{I} is not dependent on Ψ angle, meaning that it will only shift the prediction of $d_{hkil}(\Phi, \Psi)$ to greater or lower values, similar to effect of $d_{hkil,0}$. Since both $d_{hkil,0}$ and σ_{22}^{I} are used for fitting it can happen that unreasonable value for both parameters is found as result of the procedure.

5. Modeling results

Earlier, results from monotonic, room temperature, quasi-static tension tests in the RD and TD carried out on the bimodal FG and UFG ZK60 before and after rolling showed significant plastic anisotropy in the tensile response after subsequent IR passes to $e = 0.91$ and $e = 1.6$ (Fig. 6c and d). Plastic anisotropy can originate from grain morphology, texture, residual stress, and the second-phase precipitates. Fig. 2 shows that this material has an equiaxed grain structure. This, in fact, would intuitively rule out any significant contribution to plastic anisotropy from the grain morphology. The initial texture of this material, as shown in Fig. 3b, is symmetric with respect RD and TD loading, suggesting that texture alone also would not give rise to a difference in the

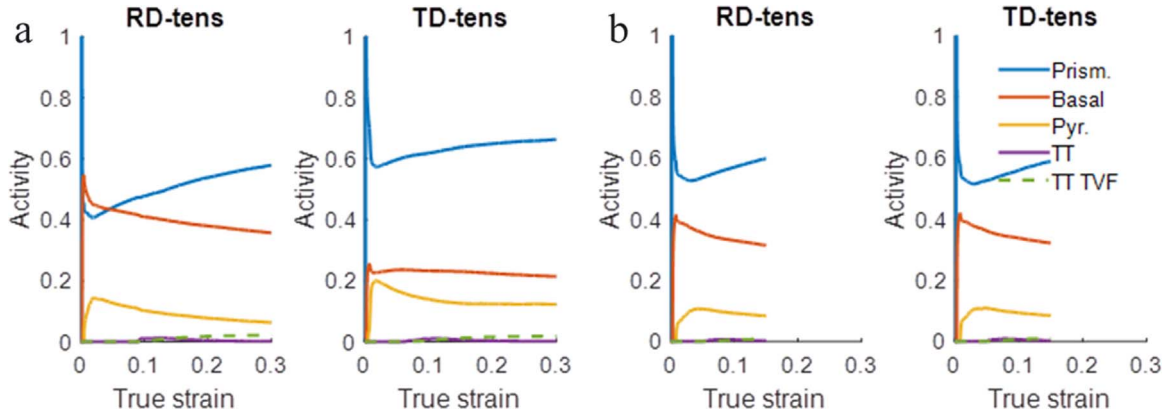

Fig. 7. Simulated relative activities during RD and TD tension after (a) MIF and (b) IR to a true strain of 0.51.

RD and TD responses.

The EPSC model is first employed to study the contribution of grain shape and texture to plastic anisotropy. These model simulations were performed under the same applied deformation conditions. The material parameters were determined by fitting the measured responses only of the MIF material (Fig. 6a). Table 4 shows the resulting parameters. For simulations of the IR passes, the same parameters were used. The initial dislocation density at the start of the IR simulations was set higher than those for the MIF simulations. This setting was motivated by the high value of dislocation density measured after hot rolling of ZK60 reported in [73].

The model calculations for all cases, both MIF and IR, are also presented in Fig. 6 to compare with the experimental measurements. Undoubtedly, the model calculations do not achieve good agreement with the data. In the model only texture and grain morphology effects were taken into account. This supports the notion mentioned above that the equiaxed grain structure and symmetric texture of this material would not be expected to lead to plastic anisotropy.

The model output for the slip activity after MIF are shown in Fig. 7a and after the first rolling in Fig. 7b. The most active slip mode before and after rolling is predicted to be prismatic < **a** > slip. Compared to prismatic slip, basal and pyramidal slip were the second and third active (~ 0.3 and ~ 0.2) systems in all samples apart from the MIF sample in TD tension, in which pyramidal slip was the second most active (~ 0.2). Twinning activity was very small (less 0.05) once the deformation strains exceeded 0.05. These results provide the first sign that the basal slip system was harder to activate than prismatic slip.

As support, we recall the particular anisotropic plastic response in the deformation of the MIF material, and in particular the higher flow stress in RD tension than TD tension. Based on the model predictions of the slip activities, basal slip was much more active in RD tension than TD tension during deformation of the MIF sample. In other words, in order to achieve agreement with the experiment, basal slip had to be much more active in RD tension. As shown in Table 3 and discussed in the model, the effects of Orowan hardening and Taylor hardening are implicitly incorporated in the initial slip resistance (Table 3). Based on Taylor hardening alone, basal slip would be easier than prismatic. However, Orowan hardening and geometry of the plate-like precipitates on the prismatic plane would make the basal planes hardened significantly over that due to Taylor hardening alone. Higher resistances in basal slip appears to be needed to predict the plastic anisotropy after MIF.

The slip activities in RD tension (Fig. 7a) after MIF and in RD and TD tension (Fig. 7b) after IR are very similar. Only the slip activities after TD tension are distinct from the other deformation cases. Thus geometric effects, or texture, could have partially contributed to the plastic anisotropy measured after MIF, but not to the anisotropy seen in the experiment in the IR samples must then not be governed by the texture.

Table 3
Constitutive parameters for evolution of slip and twin resistances established by simulating the true stress-true strain response after MIF.

	$\alpha = 1$ Prismatic	$\alpha = 2$ Basal	$\alpha = 3$ Pyramidal < c +a >
$b^{\alpha}[m]$	3.2094×10^{-10}	3.2094×10^{-10}	6.11986×10^{-10}
$\tau_0^{\alpha}[MPa]$(298 K)	10	30	50
$\tau_0^{\alpha}[MPa]$(498 K)	7	20	30
HP^{α}	40	40	40
$k_1^{\alpha}[m^{-1}]$	1.0×10^{8}	2.0×10^{8}	4.2×10^{8}
g^{α}	0.0083	0.0183	0.0145
$D^{\alpha}[MPa]$	300	1300	8300
q^{α}	4	4	4
$\dot{\varepsilon}_0^{\alpha}[s^{-1}]$	10^{7}	10^{7}	10^{7}
$\rho_{for}^{\alpha}[m^{-2}]$(MIF)	1.0×10^{12}	1.0×10^{12}	1.0×10^{12}
$\rho_{for}^{\alpha}[m^{-2}]$(MIF + $e = 0.51$)	8.0×10^{12}	8.0×10^{12}	8.0×10^{12}
$\rho_{for}^{\alpha}[m^{-2}]$(MIF + $e = 0.91$)	17.0×10^{12}	17.0×10^{12}	17.0×10^{12}
$\rho_{for}^{\alpha}[m^{-2}]$(MIF + $e = 1.6$)	25.0×10^{12}	25.0×10^{12}	25.0×10^{12}
$\rho_{debr}^{\alpha}[m^{-2}]$(MIF)	1.0×10^{-1}	1.0×10^{-1}	1.0×10^{-1}
$\rho_{debr}^{\alpha}[m^{-2}]$(MIF + $e = 0.51$)	1.0×10^{7}	1.0×10^{7}	1.0×10^{7}
$\rho_{debr}^{\alpha}[m^{-2}]$(MIF + $e = 0.91$)	1.0×10^{8}	1.0×10^{8}	1.0×10^{8}
$\rho_{debr}^{\alpha}[m^{-2}]$(MIF + $e = 1.6$)	5.0×10^{8}	5.0×10^{8}	5.0×10^{8}
Grain size [μm]	Given in Table 1.		

		$\beta = 1$ Tensile twinning
$b^{\beta}[m]$		2.47×10^{-11}
$\tau_0^{\beta}[MPa]$		135
HP^{β}		200
$C^{\alpha\beta}$	$\alpha = 1$	1000.0
	$\alpha = 2$	1000.0
	$\alpha = 3$	1300.0

5.1. Estimating residual stress at the end of MIF + IR with $e = 1.6$

As mentioned, accounting for texture alone cannot explain the plastic anisotropy in the yield stress after MIF and IR and the discrepancy between the model and experiment. Next, we considered the coupled effect of texture and development of residual stresses during processing. With the present EPSC model, a prediction of the type II residual stresses, $\langle \varepsilon^{II,d}(\Phi, \Psi, hkil) \rangle$, given in (32), can be provided. Table 4 presents the type II residual stress values calculated from the EPSC model. To obtain them, the simulation of IR from $e = 0.9$–1.6 was performed assuming the following sequence of steps: heating to 200 °C, followed by plane strain compression, and finally cooling to

Table 4
Estimated residual stress values and fitted parameters.

$\sigma_{11}^{I}[MPa]$ $(-10\ \text{MPa} < \sigma_{11}^{I} < 10\ \text{MPa})$	$\sigma_{22}^{I}[MPa](-10\ \text{MPa} < \sigma_{22}^{I} < 10\ \text{MPa})$	q $(0.07 < q < 1.0)$	$d_{hkil,0}$ [Å] $(0.85\ \text{Å} < d_{hkil,0} < 0.95\ \text{Å})$
−1.09	−4.95	0.07	0.895289

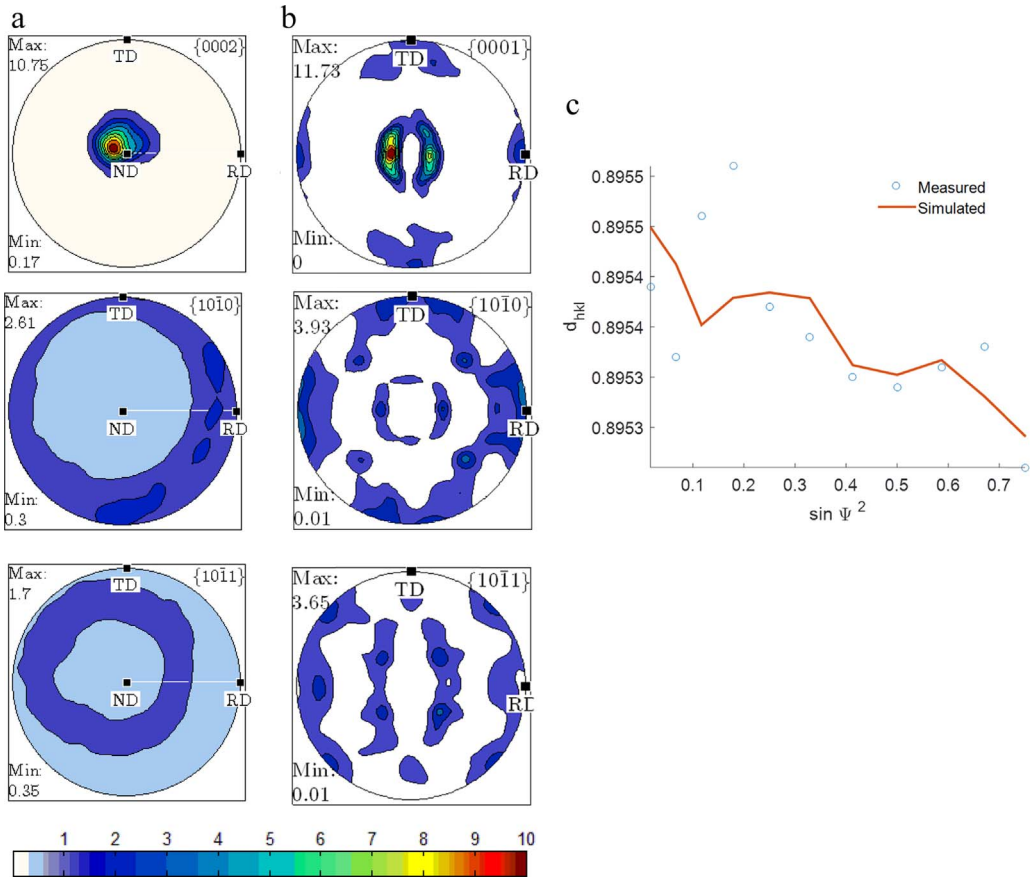

Fig. 8. Predicted (a) and measured (b) texture after IR at a true strain of 1.6 and the least square fit to measured inter-planar spacing (c).

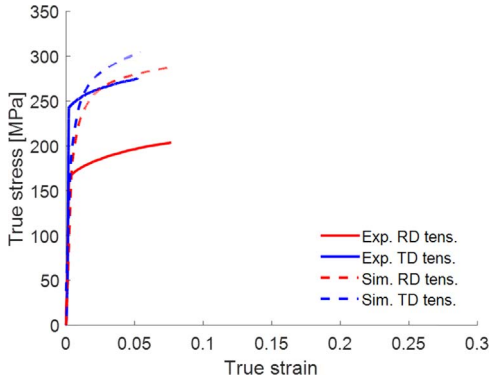

Fig. 9. Experimental flow curves after rolling to 1.6 strain compared against predicted curves including type II residual stress.

room temperature. The starting texture was the measured texture after rolling to $e = 0.9$. The values of the CRSS were changed to reflect the effect of temperature (Table 3). Comparison of predicted texture with measured after IR to 1.6 is shown in Fig. 8. Diffraction elastic constants, $F_{ij}(\Phi, \Psi, hkil)$, were evaluated for predicted texture at $e = 1.6$. The least squares fit for the experimentally measured inter-planar spacing was carried out by varying the normal stress in RD and TD, scaling parameter q and stress-free inter-planar spacing within the bounds given in Table 4 in parenthesis next to each parameter.

To evaluate the bounds on σ_{11}^{I} and $d_{hkil,0}$ we set $\sigma_{22}^{I} = 0MPa$ and $q = 0$, meaning that uniaxial type I residual stress state is assumed and that the type II residual stresses are neglected. Although gross assumptions, they allow determining the order of magnitude of σ_{11}^{I}. To set the same bounds, σ_{11}^{I} and σ_{22}^{I} are set to be similar in value, which seems to be a reasonable assumption considering previous works [71]. The bounds for q are based on previous work, while those for $d_{hkil,0}$ are made broad, so that it can be considered unconstrained. The volume average of predicted absolute type II residual stress in sample frame scaled with q is:

$$\langle \boldsymbol{\sigma}^{\mathrm{II}} \rangle = \begin{bmatrix} 4.25 & 3.6 & 5.39 \\ 3.6 & 4.32 & 3.54 \\ 5.39 & 3.54 & 5.42 \end{bmatrix} \mathrm{MPa}. \tag{34}$$

Next the calculations are performed using the predicted type I residual stresses scaled with q and predicted texture at the end of simulated IR from 0.91 to 1.6 as a starting state for tension in RD and TD directions. The results shown in Fig. 9 suggested that the error in the predicted anisotropy is likely not due to any inaccuracies in the residual stress prediction. but likely in the texture prediction. Taken together, the calculations suggest that, accounting for the evolution of residual stress, texture, hardening, and grain shape in EPSC was not capable of predicting the plastic anisotropy after IF (see Fig. 7). One effect on considered thus far is the effect of precipitate distribution. This discrepancy in the EPSC prediction for plastic anisotropy and the experiment suggests that the origin of anisotropy likely lies in the second-

phase precipitates.

6. Anisotropy hardening analysis

We note that thus far the EPSC calculation did not explicitly account for precipitation hardening. However we made the basal slip resistance harder than the prismatic slip resistance, which implicitly takes into account the effect of precipitates. Based on prior work, the tendency of second-phase precipitates is to lower the plastic anisotropy not enhance it. In very fine-grained Mg alloys, a lower plastic anisotropy can be attributed to similar activities by the basal and prismatic slip systems [31–33]. For ZK60 alloy after the standard T6 heat treatment an increase of 20–25% in strength over the as-cast material [4], was attributed to second-phase precipitates. These precipitates in the coarse-grain non-textured material did not, however, influence anisotropic strengthening. Single crystal tests on an Mg-Zn alloy, where Zn is in solid solution, showed that the effect of increasing Zn concentrations is to increase the CRSS for basal slip and decrease the CRSS for prismatic slip [74,75]. Polycrystals of this same material with grain sizes below 50 μm did not see this trend [33]. Therefore, reducing the grain size and increasing the content of Zn in solid solution and adding precipitates usually leads to lower CRSS ratios between prismatic and basal slip.

According to [76,77] Orowan strengthening was found to be more appropriate in predicting the strengthening of the CRSS for prismatic slip. It this case prismatic plane CRSS $\tau = 13$ MPa (Table 3) increase was $\sim$ 5/6 MPa after rolling with strain $e = 0.5$, 11/10 and 13/11 MPa after rolling with strain $e = 0.9$ and $e = 1.6$ in RD/TD respectively. Therefore, rolling to strains of $e = 0.9$ and more can significantly reduce prismatic slip activity.

The EPSC model of Mg alloy ZK60 did not consider the evolution precipitate geometry on various slip modes. We note that the model achieved good agreement with the macroscopic hardening after MIF and subsequence rolling with $e = 0.51$ (Fig. 7a, b). However not after rolling to $e = 0.91$ and $e = 1.6$ (Fig. 7c, d), when the change in the precipitate geometry makes the greatest difference. At these high strains, the area fraction of the precipitates S_β value had increased from 6% to nearly 12% and in size to 110–130 nm (Table 2), essentially becoming large disk-shaped precipitates. At the same time, they had become highly oriented in the RD plane. As such they become effective in strengthening the material. The strengthening, however, is anisotropic as their orientation with respect to the textures suggests that they would pose the largest barrier to $< \mathbf{c}+\mathbf{a} >$ slip, compared to basal and prismatic $< \mathbf{a} >$ slip. This leads to our key result is that the plastic anisotropy after MIF is not due to precipitate strengthening alone but due to the morphology of the precipitates; that is, the fact that they become more aligned in the RD plane during IR at 200 °C. It is this alignment that leads to a noticeable switch in yield anisotropy, causing strengthening in tensile yield stress in the TD over that in the RD.

7. Conclusions

In this work, the microstructure, crystallographic texture, and strength of the Mg-Zn-Zr (ZK60 or MA14) alloy after three-step isothermal multi-step forging (MIF) and subsequent isothermal rolling (IR) have been investigated. Based on experimental characterization and modeling, the following conclusions are drawn:

1. It is demonstrated that the chosen processing schedule, combining two different deformation techniques, is effective for fabricating fine-grained ZK60. The MIF of the hot-pressed rod performed at 200 °C with a total strain of $\sim$ 10.2 produces a fine-grained microstructure with 90% volume fraction of recrystallized grains approximately 3 μm in diameter. Subsequent isothermal rolling up to 1.6 equivalent strain at 200 °C further refines the average grain size down to 1.2 μm and leads to a completely recrystallized homogeneous, fine-grain microstructure.
2. The second phase constituents in the material and room temperature tensile behavior of the material after MIF and IR at 200 and 300 °C have been characterized. It is found that IR at the 300 °C enhances the strength of this alloy over the traditionally processed material in all test directions. The same deformation at the 200 °C led to preferred strengthening in the transverse direction over the rolling direction and hence increased the in-plane plastic anisotropy.
3. A polycrystal mean-field constitutive model based on the elastic-plastic self-consistent (EPSC) framework has been extended to incorporate residual stresses and is used to interpret the behavior of ZK60 alloy. We showed that with a unique set of single-crystal hardening parameters the model could reproduce the observed anisotropic hardening, evolution of twin volume fraction, and texture during subsequent tension testing after MIF and a subsequent rolling step. The EPSC modeling provided predictions of the residual lattice strains and residual stresses after rolling, the latter of which did not exceed 5 MPa. Thus, the magnitude of the residual stresses did not influence the plastic anisotropy of the alloy. However after further rolling, when the change in the precipitate geometry makes the greatest difference the model without the evolution of the precipitate geometry could not reproduce the observed anisotropic hardening. Multiple strengthening factors were considered in the model to interpret the observed mechanical behavior after deformation.
4. The main reason for the increase in the plastic anisotropy after rolling is the change in precipitate distribution. A sequence of forging and rolling at a temperature of 200 °C causes decomposition of the zinc in magnesium resulting in an area fraction increase of the secondary β–phase from 3 − 4 to 13 − 15%. With dynamic aging rolling, the precipitates are reshaped into the form of plates, being elongated further in the rolling direction and closely spaced.

Acknowledgements

M.K and M.Z. were supported by the U.S. National Science Foundation (NSF) under grant No. CMMI-1727495. I.J.B. was supported by the U.S. National Science Foundation (NSF) under grant No. CMMI-1728224.

References

[1] E.F. Horst, B. Mordike, Magnesium Technology. Metallurgy, Design Data, Application, Springer-Verlag, Berlin Heidelberg, Germany, 2006.
[2] Magnesium's Tough Strength Endures Abuse To Protect Portable Electronic Devices, International Magnesium Association, 2008.
[3] Boeing 787 from the Ground Up, Aero Magazine, Boeing, 4th quarter.
[4] B.L. Mordike, T. Ebert, Magnesium: properties – applications – potential, Mater. Sci. Eng. A 302 (2001) 37–45.
[5] M.M. Avedesian, H. Baker, Magnesium and Magnesium Alloys – ASM Speciality Handbook, ASM International, Materials Park, Ohio, 1999.
[6] C.S. Roberts, Magnesium and Its Alloys, Wiley, New York/London, 1960.
[7] M.R. Barnett, Twinning and the ductility of magnesium alloys: Part I: "tension" twins, Mater. Sci. Eng. A 464 (2007) 1–7.
[8] E.W. Kelly, W.F. Hosford, Plane-strain compression of magnesium and magnesium alloy crystals, Trans. Metall. Soc. AIME 242 (1968) 5–13.
[9] M.H. Yoo, Slip, twinning, and fracture in hexagonal close-packed metals, Metall. Mater. Trans. A 12 (1981) 409–418.
[10] B.C. Wonsiewicz, W.A. Backofen, Plasticity of magnesium crystals, Trans. Metall. Soc. AIME 239 (1967).
[11] M. Ardeljan, I.J. Beyerlein, B.A. McWilliams, M. Knezevic, Strain rate and temperature sensitive multi-level crystal plasticity model for large plastic deformation behavior: application to AZ31 magnesium alloy, Int. J. Plast. 83 (2016) 90–109.
[12] M. Ardeljan, I.J. Beyerlein, M. Knezevic, Effect of dislocation density-twin interactions on twin growth in AZ31 as revealed by explicit crystal plasticity finite element modeling, Int. J. Plast. 99 (2017) 81–101.
[13] M. Knezevic, A. Levinson, R. Harris, R.K. Mishra, R.D. Doherty, S.R. Kalidindi, Deformation twinning in AZ31: influence on strain hardening and texture evolution, Acta Mater. 58 (2010) 6230–6242.
[14] M. Knezevic, M.R. Daymond, I.J. Beyerlein, Modeling discrete twin lamellae in a microstructural framework, Scr. Mater. 121 (2016) 84–88.
[15] T. Obara, H. Yoshinga, S. Morozumi, 11-22 < −1-123 > slip system in magnesium, Acta Metall. 21 (1973) 845–853.
[16] S. Agnew, M. Yoo, C. Tome, Application of texture simulation to understanding mechanical behavior of Mg and solid solution alloys containing Li or Y, Acta Mater. 49 (2001) 4277–4289.

[17] J.D. Robson, C. Paa-Rai, The interaction of grain refinement and ageing in magnesium–zinc–zirconium (ZK) alloys, Acta Mater. 95 (2015) 10–19.
[18] Y. Estrin, A. Vinogradov, Extreme grain refinement by severe plastic deformation: a wealth of challenging science, Acta Mater. 61 (2013) 782–817.
[19] S. Zherebtsov, M. Murzinova, G. Salishchev, S. Semiatin, Spheroidization of the lamellar microstructure in Ti–6Al–4V alloy during warm deformation and annealing, Acta Mater. 59 (2011) 4138–4150.
[20] A. Jain, O. Duygulu, D.W. Brown, C.N. Tomé, S.R. Agnew, Grain size effects on the tensile properties and deformation mechanisms of a magnesium alloy, AZ31B, sheet, Mater. Sci. Eng. A 486 (2008) 545–555.
[21] W. Chen, X. Wang, L. Hu, E. Wang, Fabrication of ZK60 magnesium alloy thin sheets with improved ductility by cold rolling and annealing treatment, Mater. Des. 40 (2012) 319–323.
[22] X. Li, T. Al-Samman, G. Gottstein, Mechanical properties and anisotropy of ME20 magnesium sheet produced by unidirectional and cross rolling, Mater. Des. 32 (2011) 4385–4393.
[23] H.K. Lim, D.H. Kim, J.Y. Lee, J.S. Kyeong, W.T. Kim, D.H. Kim, Effects of rolling condition on the tensile properties of Mg-MM-Sn-Al-Zn alloy, Met. Mater. Int. 15 (2009) 337–343.
[24] M. Barnett, N. Stanford, P. Cizek, A. Beer, Z. Xuebin, Z. Keshavarz, Deformation mechanisms in Mg alloys and the challenge of extending room-temperature plasticity, JOM 61 (2009) 19–24.
[25] J. Del Valle, F. Carreño, O.A. Ruano, Influence of texture and grain size on work hardening and ductility in magnesium-based alloys processed by ECAP and rolling, Acta Mater. 54 (2006) 4247–4259.
[26] P. Dobroň, F. Chmelík, S. Yi, K. Parfenenko, D. Letzig, J. Bohlen, Grain size effects on deformation twinning in an extruded magnesium alloy tested in compression, Scr. Mater. 65 (2011) 424–427.
[27] J. Wang, N. Stanford, Investigation of precipitate hardening of slip and twinning in Mg5% Zn by micropillar compression, Acta Mater. 100 (2015) 53–63.
[28] N. Stanford, J. Geng, Y. Chun, C. Davies, J. Nie, M. Barnett, Effect of plate-shaped particle distributions on the deformation behavior of magnesium alloy AZ91 in tension and compression, Acta Mater. 60 (2012) 218–228.
[29] M. Lentz, M. Klaus, M. Wagner, C. Fahrenson, I.J. Beyerlein, M. Zecevic, W. Reimers, M. Knezevic, Effect of age hardening on the deformation behavior of an Mg–Y–Nd alloy: in-situ X-ray diffraction and crystal plasticity modeling, Mater. Sci. Eng. A 628 (2015) 396–409.
[30] M. Lentz, M. Klaus, R.S. Coelho, N. Schaefer, F. Schmack, W. Reimers, B. Clausen, Analysis of the deformation behavior of magnesium-rare earth alloys Mg-2 pct Mn-1 pct rare earth and Mg-5 pct Y-4 pct rare earth by in situ energy-dispersive x-ray synchrotron diffraction and elasto-plastic self-consistent modeling, Metall. Mater. Trans. A 45 (2014) 5721–5735.
[31] J. Koike, Enhanced deformation mechanisms by anisotropic plasticity in polycrystalline Mg alloys at room temperature, Metall. Mater. Trans. A 36 (2005) 1689–1696.
[32] J. Koike, T. Kobayashi, T. Mukai, H. Watanabe, M. Suzuki, K. Maruyama, K. Higashi, The activity of non-basal slip systems and dynamic recovery at room temperature in fine-grained AZ31B magnesium alloys, Acta Mater. 51 (2003) 2055–2065.
[33] N. Stanford, M.R. Barnett, Solute strengthening of prismatic slip, basal slip and twinning in Mg and Mg–Zn binary alloys, Int. J. Plast. 47 (2013) 165–181.
[34] M. Ardeljan, D.J. Savage, A. Kumar, I.J. Beyerlein, M. Knezevic, The plasticity of highly oriented nano-layered Zr/Nb composites, Acta Mater. 115 (2016) 189–203.
[35] J. Nie, Effects of precipitate shape and orientation on dispersion strengthening in magnesium alloys, Scr. Mater. 48 (2003) 1009–1015.
[36] M. Jahedi, B.A. McWilliams, P. Moy, M. Knezevic, Deformation twinning in rolled WE43-T5 rare earth magnesium alloy: influence on strain hardening and texture evolution, Acta Mater. 131 (2017) 221–232.
[37] X. Gao, J.F. Nie, Characterization of strengthening precipitate phases in a Mg–Zn alloy, Scr. Mater. 56 (2007) 645–648.
[38] N. Stanford, M.R. Barnett, Effect of particles on the formation of deformation twins in a magnesium-based alloy, Mater. Sci. Eng.: A 516 (2009) 226–234.
[39] D. Xu, L. Liu, Y. Xu, E. Han, The effect of precipitates on the mechanical properties of ZK60-Y alloy, Mater. Sci. Eng. A 420 (2006) 322–332.
[40] N. Stanford, J. Geng, Y.B. Chun, C.H.J. Davies, J.F. Nie, M.R. Barnett, Effect of plate-shaped particle distributions on the deformation behavior of magnesium alloy AZ91 in tension and compression, Acta Mater. 60 (2012) 218–228.
[41] S. Kok, A.J. Beaudoin, D.A. Tortorelli, A polycrystal plasticity model based on the mechanical threshold, Int. J. Plast. 18 (2002) 715–741.
[42] P. Follansbee, U. Kocks, A constitutive description of the deformation of copper based on the use of the mechanical threshold stress as an internal state variable, Acta Metall. 36 (1988) 81–93.
[43] I.J. Beyerlein, R.J. McCabe, C.N. Tome, Stochastic processes of 1012 deformation twinning in hexagonal close-packed polycrystalline zirconium and magnesium, Int. J. Multiscale Comput. Eng. 9 (2011) 459–480.
[44] I.J. Beyerlein, C.N. Tomé, A dislocation-based constitutive law for pure Zr including temperature effects, Int. J. Plast. 24 (2008) 867–895.
[45] M. Zecevic, I.J. Beyerlein, M. Knezevic, Coupling elasto-plastic self-consistent crystal plasticity and implicit finite elements: applications to compression, cyclic tension-compression, and bending to large strains, Int. J. Plast. 93 (2017) 187–211.
[46] S. Ghorbanpour, M. Zecevic, A. Kumar, M. Jahedi, J. Bicknell, L. Jorgensen, I.J. Beyerlein, M. Knezevic, A crystal plasticity model incorporating the effects of precipitates in superalloys: application to tensile, compressive, and cyclic deformation of Inconel 718, Int. J. Plast. 99 (2017) 162–185.
[47] M. Zecevic, Y.P. Korkolis, T. Kuwabara, M. Knezevic, Dual-phase steel sheets under cyclic tension–compression to large strains: experiments and crystal plasticity modeling, J. Mech. Phys. Solids 96 (2016) 65–87.
[48] G. Proust, C.N. Tomé, G.C. Kaschner, Modeling texture, twinning and hardening evolution during deformation of hexagonal materials, Acta Mater. 55 (2007) 2137–2148.
[49] M. Knezevic, L. Capolungo, C.N. Tomé, R.A. Lebensohn, D.J. Alexander, B. Mihaila, R.J. McCabe, Anisotropic stress-strain response and microstructure evolution of textured α-uranium, Acta Mater. 60 (2012) 702–715.
[50] M. Knezevic, I.J. Beyerlein, D.W. Brown, T.A. Sisneros, C.N. Tomé, A polycrystal plasticity model for predicting mechanical response and texture evolution during strain-path changes: application to beryllium, Int. J. Plast. 49 (2013) 185–198.
[51] D.R. Nugmanov, O.S. Sitdikov, M.V. Markushev, Microstructure evolution in MA14 magnesium alloy under multi-step isothermal forging, Lett. Mater. 1 (2011) 213–216.
[52] D.R. Nugmanov, O.S. Sitdikov, M.V. Markushev, Structure of magnesium alloy MA14 after multistep isothermal forging and subsequent isothermal rolling, Phys. Met. Metallogr. 116 (2015) 993–1001.
[53] L. Utevskii. Diffraction Electron Microscopy in Materials Science, Metallurgiya, Moscow.
[54] D. Nugmanov, O.S. Sitdikov, M. Markushev, The second phase behavior in magnesium alloy MA14 under multistep isothermal forging and further isothermal rolling, Lett. Mater. 7 (2017) 198–202.
[55] X. Gao, J. Nie, Characterization of strengthening precipitate phases in a Mg–Zn alloy, Scr. Mater. 56 (2007) 645–648.
[56] J. Robson, N. Stanford, M. Barnett, Effect of precipitate shape on slip and twinning in magnesium alloys, Acta Mater. 59 (2011) 1945–1956.
[57] P.A. Turner, C.N. Tomé, A study of residual stresses in Zircaloy-2 with rod texture, Acta Metall. Mater. 42 (1994) 4143–4153.
[58] J.D. Eshelby, The determination of the elastic field of an ellipsoidal inclusion, and related problems, Proc. R. Soc. Lond. A 241 (1957) 376–396.
[59] U.F. Kocks, C.N. Tomé, H.-R. Wenk, Texture and Anisotropy, Cambridge University Press, Cambridge, UK, 1998.
[60] M. Zecevic, M. Knezevic, I.J. Beyerlein, C.N. Tomé, An elasto-plastic self-consistent model with hardening based on dislocation density, twinning and de-twinning: application to strain path changes in HCP metals, Mater. Sci. Eng. A 638 (2015) 262–274.
[61] M. Zecevic, M. Knezevic, A dislocation density based elasto-plastic self-consistent model for the prediction of cyclic deformation: application to Al6022-T4, Int. J. Plast. 72 (2015) 200–217.
[62] M. Knezevic, M. Zecevic, I.J. Beyerlein, J.F. Bingert, R.J. McCabe, Strain rate and temperature effects on the selection of primary and secondary slip and twinning systems in HCP Zr, Acta Mater. 88 (2015) 55–73.
[63] M. Lentz, M. Klaus, I.J. Beyerlein, M. Zecevic, W. Reimers, M. Knezevic, In situ X-ray diffraction and crystal plasticity modeling of the deformation behavior of extruded Mg–Li–(Al) alloys: an uncommon tension–compression asymmetry, Acta Mater. 86 (2015) 254–268.
[64] U. Essmann, H. Mughrabi, Annihilation of dislocations during tensile and cyclic deformation and limits of dislocation densities, Philos. Mag. A 40 (1979) 731–756.
[65] H. Mecking, U.F. Kocks, Kinetics of flow and strain-hardening, Acta Metall. Mater. 29 (1981) 1865–1875.
[66] U.F. Kocks, H. Mecking, Physics and phenomenology of strain hardening: the FCC case, Prog. Mater. Sci. 48 (2003) 171–273.
[67] B. Clausen, C.N. Tomé, D.W. Brown, S.R. Agnew, Reorientation and stress relaxation due to twinning: modeling and experimental characterization for Mg, Acta Mater. 56 (2008) 2456–2468.
[68] P. Withers, H. Bhadeshia, Residual stress. Part 1–measurement techniques, Mater. Sci. Technol. 17 (2001) 355–365.
[69] A. Baczmański, C. Braham, W. Seiler, Microstresses in textured polycrystals studied by the multireflection diffraction method and self-consistent model, Philos. Mag. 83 (2003) 3225–3246.
[70] A. Baczmański, K. Wierzbanowski, P. Lipiński, R. Helmholdt, G. Ekambaranathan, B. Pathiraj, Examination of the residual stress field in plastically deformed polycrystalline material, Philos. Mag. A 69 (1994) 437–449.
[71] D. Gloaguen, T. Berchi, E. Girard, R. Guillén, Measurement and prediction of residual stresses and crystallographic texture development in rolled Zircaloy-4 plates: x-ray diffraction and the self-consistent model, Acta Mater. 55 (2007) 4369–4379.
[72] D. Gloaguen, T. Berchi, E. Girard, R. Guillen, Examination of residual stresses and texture in zirconium alloy cladding tubes after a large plastic deformation: experimental and numerical study, J. Nucl. Mater. 374 (2008) 138–146.
[73] H. Chen, Q. Zang, H. Yu, J. Zhang, Y. Jin, Effect of intermediate annealing on the microstructure and mechanical property of ZK60 magnesium alloy produced by twin roll casting and hot rolling, Mater. Charact. 106 (2015) 437–441.
[74] A. Akhtar, E. Teghtsoonian, Solid solution strengthening of magnesium single crystals—I alloying behavior in basal slip, Acta Metall. 17 (1969) 1339–1349.
[75] A. Akhtar, E. Teghtsoonian, Solid solution strengthening of magnesium single crystals—II the effect of solute on the ease of prismatic slip, Acta Metall. 17 (1969) 1351–1356.
[76] F. Wang, J.J. Bhattacharyya, S.R. Agnew, Effect of precipitate shape and orientation on Orowan strengthening of non-basal slip modes in hexagonal crystals, application to magnesium alloys, Mater. Sci. Eng. A 666 (2016) 114–122.
[77] J. Jain, P. Cizek, W.J. Poole, M.R. Barnett, Precipitate characteristics and their effect on the prismatic-slip-dominated deformation behavior of an Mg–6 Zn alloy, Acta Mater. 61 (2013) 4091–4102.